

Article

Not peer-reviewed version

A Core and Valence Level Spectroscopy Study of the Enhanced Reduction of CeO₂ by Iron Substitution. Implication on the Thermal Water Splitting Reaction.

[Hicham Idriss](#) *

Posted Date: 22 December 2023

doi: 10.20944/preprints202312.1685.v1

Keywords: Cerium oxide reduction; Cerium cation substitution; X-ray valence band spectroscopy; thermogravimetric analysis; XPS Ce4f; XPS Fe2p



Preprints.org is a free multidiscipline platform providing preprint service that is dedicated to making early versions of research outputs permanently available and citable. Preprints posted at Preprints.org appear in Web of Science, Crossref, Google Scholar, Scilit, Europe PMC.

Copyright: This is an open access article distributed under the Creative Commons Attribution License which permits unrestricted use, distribution, and reproduction in any medium, provided the original work is properly cited.

Article

A Core and Valence Level Spectroscopy Study of the Enhanced Reduction of CeO₂ by Iron Substitution: Implication on the Thermal Water Splitting Reaction

Hicham Idriss

Institute of Functional Interfaces, Karlsruhe Institute of Technology (KIT), 76344 Eggenstein-Leopoldshafen, Germany

Abstract: The reduction of Ce cations in CeO₂ can be enhanced by its partial substitution by Fe cations. The enhanced reduction of Ce cations results in a considerable increase in the reaction rates for thermal water splitting reaction when compared to CeO₂ alone. This mixed oxide has a smaller crystallite size when compared to CeO₂ in addition to a smaller lattice size. In this work, two Fe-substituted Ce oxides are studied (Ce_{0.95}Fe_{0.05}O₂ and Ce_{0.75}Fe_{0.25}O₂) by core and valence level spectroscopy in their as-prepared and Ar-ions sputtered states. Ar-ions sputtering substantially increases Ce4f lines at about 1.5 eV below the Fermi level. In addition, it is found that the XPS Ce5p/O2s ratio is sensitive to the degree of reduction, most likely due to a higher charge transfer from the oxygen to Ce ions upon reduction. Quantitatively it is also found that XPS Ce3d of the fraction of Ce³⁺ (u_o, u' and v_o, v') formed upon Ar-ions sputtering and the ratio Ce5p/O2s lines are higher for reduced Ce_{0.95}Fe_{0.05}O₂ than for reduced Ce_{0.75}Fe_{0.25}O₂. XPS Fe2p showed however no preferential increase for Fe³⁺ reduction to Fe⁰ with increasing time for both oxides. Since water splitting was higher on Ce_{0.95}Fe_{0.05}O₂ when compared to Ce_{0.75}Fe_{0.25}O₂, it is inferred that the reaction centers for the thermal water splitting to hydrogen are the reduced Ce cations and not the reduced Fe cations. These reduced Ce cations can be tracked by their XPS Ce5p/O2s ratio in addition to the common XPS Ce3d lines.

Keywords: Cerium oxide reduction; Cerium cation substitution; X-ray valence band spectroscopy; thermogravimetric analysis; XPS Ce4f; XPS Fe2p

1. Introduction

Cerium oxide is one of the most known stable redox oxides. This property makes it the oxide support of choice for automobile catalytic converters (three-way catalyst, TWC) which has been in implementation for decades⁰. The relative ease by which it goes through reduction and re-oxidation cycles while maintaining its crystallographic structure (fluorite) is the main reason². This particular property also makes it among the best-known support oxides for other redox catalytic reactions such as the water gas shift reaction (WGSR)³. For both reactions (WGSR and TWC) the reduction of CeO₂ occurs chemically. In other words, the input of energy is from a hydrocarbon in the case of the TWC and from CO in the case of WGSR⁴. This allows the redox cycle to occur at relatively low temperatures relevant for catalytic reactions.

CeO₂ is also one of the most active and stable known oxides for the thermochemical water splitting to H₂ and O₂; for energy applications⁵. For this reaction, however, the reduction is considered in the absence of a reducing agent and where heat (from the sun) is the sole energy input. Temperatures typically above 1500°C are needed for an appreciable reduction to take place⁶. This adds a considerable strain on the process and so far, possible applications would be very costly and largely unpractical. To this end, much work addressing the reduction of CeO₂ in order to understand its steps at the fundamental and applied levels has been pursued.

One of the strategies to enhance the reduction of CeO₂ is to mix it with other oxides. This may be grouped into three categories.

1. Size substitution (iso-valency): Compensation for lattice expansion. Upon the reduction of Ce^{4+} cations to Ce^{3+} the unit cell of CeO_2 increases. This is because the eight-coordinated Ce^{4+} cation size is about 1 Å, while the eight-coordinated Ce^{3+} cation size is about 1.1 Å. Substituting part of Ce^{4+} cations with a metal cation with the same formal oxidation state (M^{4+}) but a smaller size compensates partly for the lattice expansion. This is in particular successful when Zr^{4+} cation is used (size ca. 0.8 Å)^{Error! Reference source not found.,8}. While the substitution is valid up to about 50% (maintaining the fluorite structure of CeO_2)⁹ phase segregation occurs at high temperatures (at 1000°C or so)¹⁰.
2. Charge transfer: substitution with reducible higher valence cations. In this case, a fraction of Ce^{4+} is substituted by a metal cation that can donate an electron and itself be oxidized¹¹. The substitution of Ce^{4+} by U^{4+} was found to enhance the reduction of CeO_2 , in particular at low levels^{12,13}. Upon the removal of an oxygen atom, three Ce^{3+} cations are formed (instead of two) and one U^{4+} is oxidized to U^{5+} . In addition, the fact that both oxides CeO_2 and UO_2 have the fluorite structure and both cations have the same size, makes them miscible for the entire ratio range.¹⁴. The optimal dosing for the reduction of Ce cations is not clear yet, and neither is the temperature at which phase segregation occurs.
3. Charge compensation (alio-valencies): lattice distortion. While the substitution of Ce^{4+} with metal cations of lower oxidation will create vacancies, these vacancies are not charged. In other words, there is no increase in electron charge. The effect is however clear, for example, the substitution of Ce^{4+} by Fe^{3+} cations (up to about 20 %) results in a considerable reduction of the host oxide¹⁵. This is thought to be due to the distortion of the lattice structure making it less stable and therefore enabling further reduction¹⁶. In recent work, this was found to be the case upon high temperature reduction (with no chemical input). Yet, considerable phase segregation occurred after one TCWS reaction cycle¹⁷.

In the case of alio-valence substitution (the word substitution is sometimes mentioned as doping; strictly doping is the addition of another element in ppm or ppb amounts to change electronic properties and is not necessary added as a substitution) a large number of elements were studied and most showed that Ce^{4+} reduction to Ce^{3+} was enhanced. These include, Co (4%) co-precipitation for the photoreduction of CO_2 to CH_4 ,¹⁸ Co (23%) for COS hydrolysis¹⁹, Co (20%) for Hg removal²⁰, Pr (10-50%) in which Pr^{3+} increases the creation of oxygen vacancies and Pr^{4+} increases oxygen storage capacity²¹, and Mn (12 %) enhancing oxygen mobility via vacancy formation²². Computationally a large body of work was also conducted to study the creation of oxygen vacancies upon alio-valent cation substitution. These include the following: Mn (DFT + U and HSE06)²³, Cu (DFT + U)²⁴, Ni (DFT + U and HSE06)²⁵ and (DFT + U)²⁶, and other rare earth elements (Sc, Y, Gd, La) by DFT + U and Monte Carlo simulations²⁷.

Focusing on Fe substitution considerable work at the experimental and theoretical work has been conducted and a few are mentioned here. Fe substitution in less than 30% increased the number of oxygen vacancies²⁸ and the selective catalytic reduction of NO with NH_3 . DFT +U results of Fe-doped ceria(111) indicated that oxygen vacancy formation energy is lower when compared to ceria alone and that Fe tends to be the center of the oxygen vacancy clusters²⁹. Improved CO conversion over $\text{CeO}_2\text{-Fe}_2\text{O}_3$ mixed oxide was also seen and attributed to the formation of more mobile oxygen atoms in the redox cycle³⁰. Fe substitution was previously studied for the thermochemical water splitting among other cation substitutions (Mn, Ni, and Cu), and the CeO_2 substituted was found still active after four reaction cycles (O_2 and H_2 release)³¹ at 1273K (1000°C). In another work for the same reaction, Fe 5% was tested at 1550°C and was found to be more active (higher production rate per unit weight) and faster (higher rate of release of hydrogen) than CeO_2 alone. However, considerable phase segregation occurred, due to the very high thermal reduction, 1550°C, after one cycle of reaction¹⁷.

2. Experimental

Cerium/Iron oxide catalysts were synthesized using the co-precipitation method already presented in other work¹⁷. In brief, cerium (III) nitrate hexahydrate (Sigma Aldrich) was dissolved in deionized water along with Iron nitrate (Sigma Aldrich). Then ammonium hydroxide, used as a

precipitating agent (70%) was added to the cerium/iron mixture while stirring vigorously until the solution reached a pH of 9-10. After filtration of the precipitate it was washed using deionized water until a neutral pH was obtained. After drying the hydroxide/oxide in an oven at 100°C it was crushed, loaded into a crucible, and calcined in air at 500°C for 12 hours with a temperature ramp of 15°C min⁻¹.

X-ray diffraction (XRD) data sets were collected using a PANalytical EMPYREAN diffractometer in Bragg–Brentano geometry with Cu K α excitation at 45 kV and 40 mA and a linear position sensitive detector. The diffractometer was configured with a 0.25° diverging slit, 0.5° anti-scattering slit, 2.3° Soller slits, and a Ni filter. Data were acquired in continuous scanning mode over the 2 θ range 10–90°, using a step interval of 0.01° and a counting time of 0.5 s per step. Experiments conducted as a function of temperature were conducted in ambient conditions.

Transmission electron microscopy (TEM) studies were conducted using Titan ST microscope (FEI company) operated at an accelerating voltage of 300 kV equipped with a field emission electron gun, a 4k×4k CCD camera, a Gatan imaging filter (GIF), and Gatan microscopy suite (GMS). Scanning TEM (STEM) – Electron Energy Loss Spectroscopy (EELS) data were obtained in the dual-EELS mode which acquires low-loss (signal from valence electrons) and core-loss (signal from core-shell electrons) EELS spectra simultaneously using a high-speed electrostatic shutter. The core-loss EELS spectra provided the energy-loss edges of Fe-L_{2,3}, Ce-M_{4,5} and O-K at the values of (721, 708) eV, (901, 883) eV, and 532 eV, respectively.

X-ray photoelectron spectroscopy (XPS) was conducted using a Thermo scientific ESCALAB 250 Xi. Spectra were calibrated with respect to C1s at 284.7 eV. The Fe2p, O1s, Ce3d, Ce4d, C1s, O2s, Ce5s, Ce5p, and the valence band (O2p, Ce4f and Fe3d) binding energy regions were scanned. Typical acquisition conditions were as follows: pass energy = 20 eV and scan rate = 0.1 eV per 200 ms. Ar ion bombardment was performed with an EX06 ion gun at 1 kV beam energy and 10 mA emission current. The sputtered area of 900 × 900 μ m² was larger than the analyzed area: 600 × 600 μ m². Self-supported oxide disks of approximately 0.5 cm diameter were loaded into the chamber. Data acquisition and treatment were done using the Advantage software. Charge neutralization was used for all samples (1 eV) and all binding energies were referenced to adventitious carbon at a binding energy of 284.7 eV.

All experimental work was conducted at SABIC research centers of KAUST and Riyadh.

3. Results and Discussions

The prepared CeO₂ and Fe substituted CeO₂ were studied in some detail previously by TEM, EELS, XRD, and TPR among other methods¹⁷. Figure 1 gives a brief description of Ce_{0.95}Fe_{0.05}O₂ and Ce_{0.75}Fe_{0.25}O₂. Both oxides are composed of small crystallites upon calcination (500°C). These were about 8 and 5 nm for Ce_{0.95}Fe_{0.05}O₂ and Ce_{0.75}Fe_{0.25}O₂, respectively. TEM images show that they are dominantly (111) terminated. These crystals are identical to those of CeO₂ (not shown), which is composed of crystallites of about 14 nm in size. The decrease in the crystallite sizes upon Fe substitution is also similar to that previously reported by others.³² This is most likely due to the change in ionicity of the sol-gel medium during the precipitation³³. Also, as seen the only observed phase (XRD, TEM) is the fluorite one. The unit cells show a slight decrease due to Fe substitution (0.543, 0.539, 0.536 nm for CeO₂, Ce_{0.95}Fe_{0.05}O₂ and Ce_{0.75}Fe_{0.25}O₂, respectively). As shown in Figure 1 (C and D) up to 700°C there is a gradual small increase in the lattice and crystallite sizes. An abrupt change occurs at 900°C where considerable sintering is seen and is accompanied by the appearance of lines due to Fe oxides indicating the beginning of the phase segregation process, which was accentuated by 1100°C.

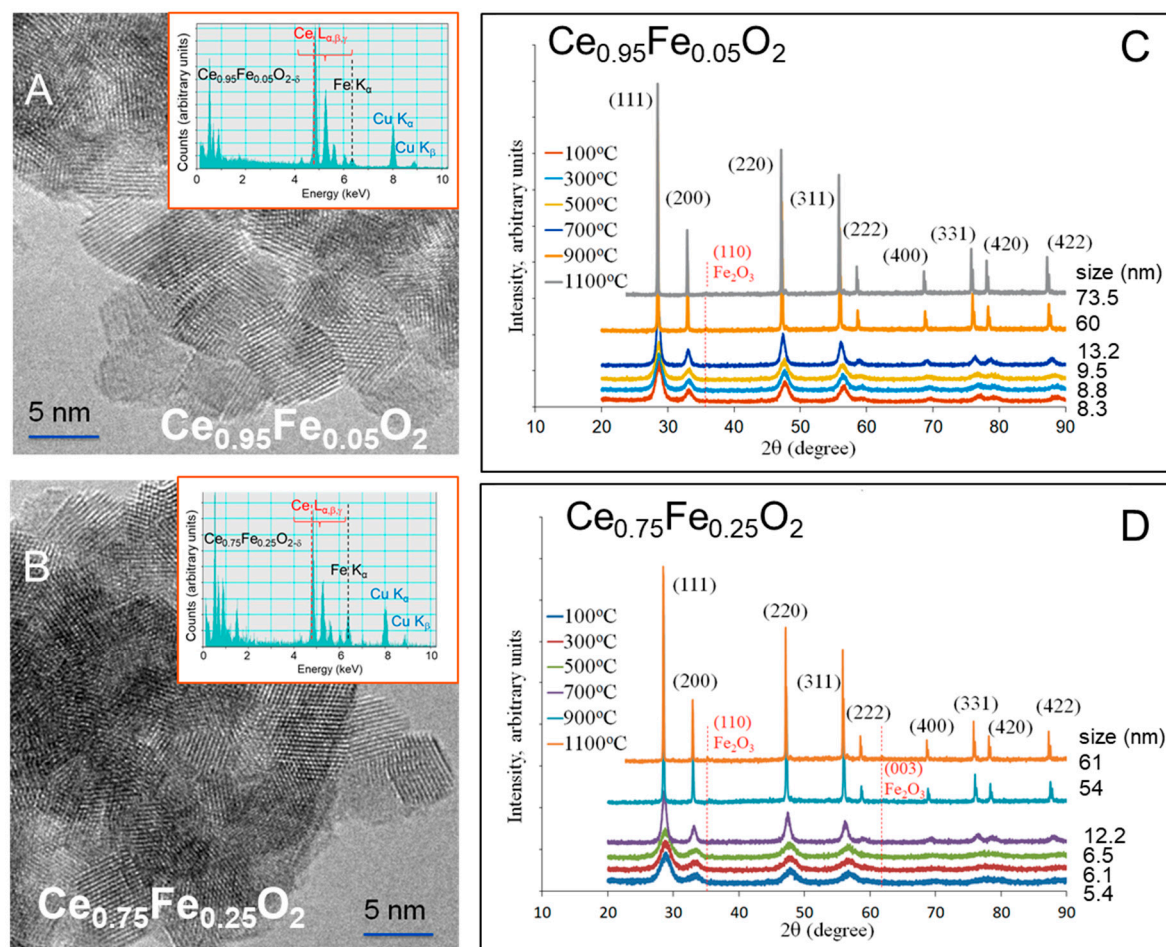


Figure 1. Transmission Electron Microscopy (TEM) (A and B), energy dispersive X-ray (EDX) (insets in A and B), and X-ray diffraction (XRD) of (C) $\text{Ce}_{0.95}\text{Fe}_{0.05}\text{O}_2$ and (D) $\text{Ce}_{0.75}\text{Fe}_{0.25}\text{O}_2$. The figures are adapted with permission from Ref. 17.

Figure 2 (A and B) presents the valence band and shallow core levels (Ce5p, O2s, and Ce5s) of $\text{Ce}_{0.75}\text{Fe}_{0.25}\text{O}_2$ and $\text{Ce}_{0.95}\text{Fe}_{0.05}\text{O}_2$ before and after 1-, 2-, and 5-minute argon ions sputtering. The initial spectra of the as-prepared oxides (0 minute) are dominated by the O2p, O2s, Ce5p, and Ce5s lines and are hardly distinguishable for both oxides. There are traces of unavoidable surface hydroxyls ($-\text{OH}$, 3) at a binding energy of ca. 10 eV and some contribution from reduced Ce cations (Ce^{4f} , Ce^{3+}) and reduced Fe cations (Fe^{3d} , oxidation state $< +3$), both below the O2p band with a binding energy of 0.5-2 eV. Upon argon ions sputtering, three changes are noticeable. (i) Increase in the signal before the O2p (due to increased concentrations of Ce^{3+} and Fe^{+x} , $x < +3$). (ii) Increase in surface hydroxyls. (iii) A relative increase in the Ce5p with respect to the O2s signals. For (i) the increase is expected and is treated in more detail in this work to extract quantitative information. For (ii) the increase has been seen before and is linked to the increase in the sticking coefficient of dissociatively adsorbed water (in the background) over a reduced metal oxide when compared to its stoichiometric form. The ion bombardment causes a reduction due to oxygen removal (as atoms) and the remaining electrons (two for each oxygen atom removed) are transferred to Ce^{4+} (and Fe^{3+}) to reduce them. The creation of the oxygen vacancy leads to preferential dissociative adsorption of a water molecule. This results in the formation of two pairs of surface hydroxyls for each oxygen vacancy healed. This is not the purpose of this study and will not be further treated. For (iii) this observation is unexpected and is treated here qualitatively.

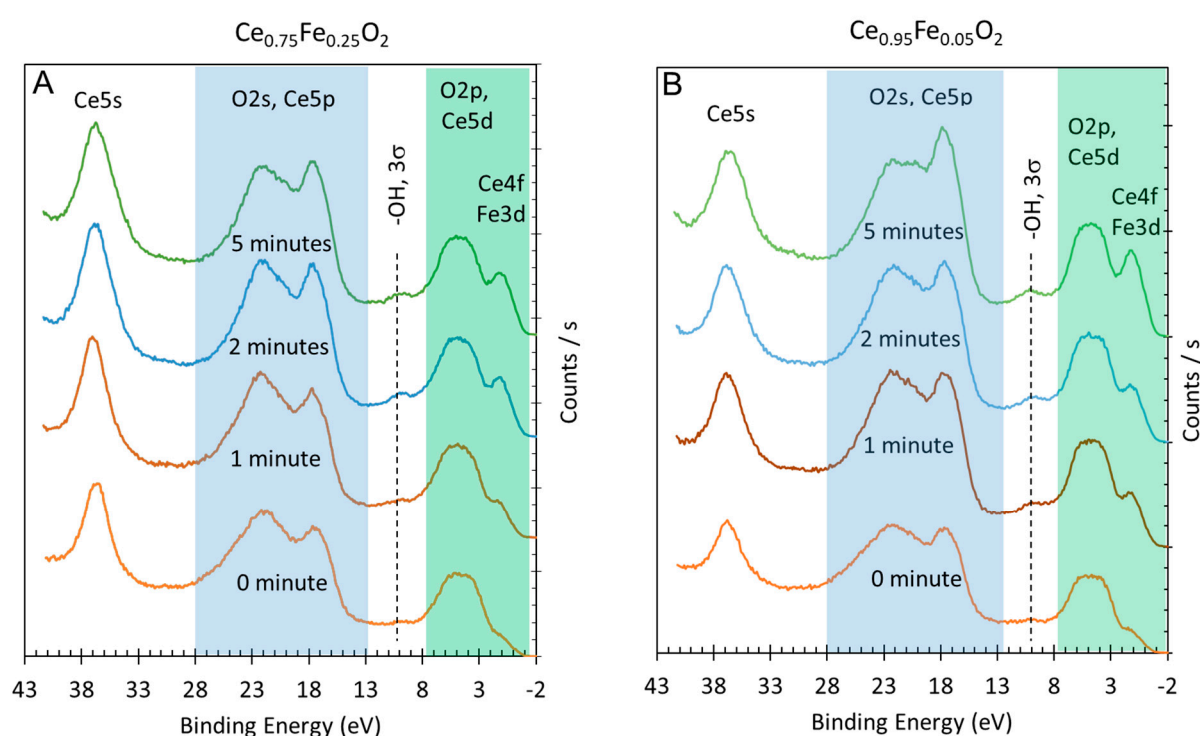


Figure 2. A. Valence band-XPS (green shaded) and Ce5p, O2s (Blue shaded), and Ce5s of $\text{Ce}_{0.75}\text{Fe}_{0.25}\text{O}_2$ before (0 minute) and after Argon ions sputtering (x minutes). B. Valence band-XPS (green shaded) and Ce5p, O2s (Blue shaded), and Ce5s of $\text{Ce}_{0.95}\text{Fe}_{0.05}\text{O}_2$ before (0 minute) and after Argon ions sputtering (x minutes).

Figure 3 (A and B) presents the valence band region, in which the signal below the O2p was fitted for two peaks. The first at about 0.4 eV and the second at ca. 1.5 eV, below the Fermi level. There are no noticeable changes in the largely O2p lines shape with sputtering time. For both oxides, the signal attributed to Ce4f is higher than that of Fe3d. The increase of Ce4f upon reduction is more pronounced in the case of low Fe concentration when compared to the other oxide. This is consistent with the other core levels (see below) as well as with the TCWS results (also see below). Computing the peak areas of the two peaks seems to indicate that there is no incentive to further reduce Ce cations with a higher % of Fe. At low % increasing reduction time affects mostly Ce cations while at Fe % it favors Fe reduction. This might be simply due to the probability of hitting the atoms during bombardment. At high Fe %, the probability of oxygen removal adjacent to Fe atoms is high, and therefore more Fe is reduced, while at low Fe % the oxide is more homogeneous and the chemical effect on the reduction has a higher effect.

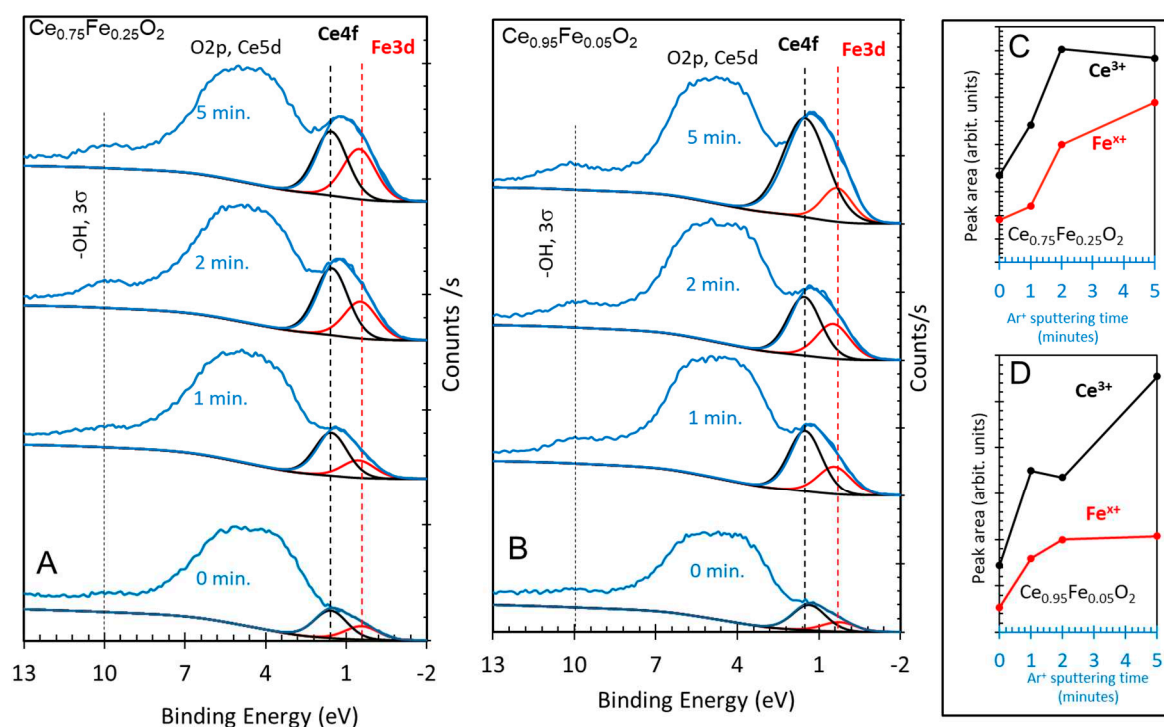


Figure 3. A. Valence band XPS of as prepared $\text{Ce}_{0.75}\text{Fe}_{0.25}\text{O}_2$ and after 1, 2, and 5-minute Ar^+ ions sputtering. B. Valence band XPS of as prepared $\text{Ce}_{0.95}\text{Fe}_{0.05}\text{O}_2$ and after 1, 2, and 5-minutes Ar^+ ions sputtering. C and D computed peak areas of fitted Ce4f (FWHM = 1.5 eV) and Fe3d (FWHM = 1.5 eV) signals.

Figure 4 (A and B) presents the valence band together with the Ce5p and O2s lines. The spectra are baseline subtracted and then normalized to highlight the differences. Ion sputtering of both oxides results in a preferential increase of the Ce5p when compared to the O2s lines. In addition, the O2s line becomes narrower upon ion sputtering. There is no noticeable shift in binding energy before or after ion bombardment. Similar experiments were conducted on CeO_2 and no change was seen (SI Figure S1). Obtaining quantitative information from polycrystalline oxides is more difficult because of the unavoidable grain boundary effect (channeling), and shadowing both would make ion sputtering less efficient when compared to sputtering thin films or single crystals. Nevertheless, some qualitative information may be drawn by comparison to previous work conducted by others. One of the most relevant to this present work is a study by ion bombardment³⁴ of CeO_2 in which it was shown (figure 3 (a and b) of ref. 34) that the relative ratio is indeed increased in favor of Ce5p. Actually, the exact position of the O2s with respect to $\text{Ce}5p_{1/2}$ is not clear. In this work, it is put after the $\text{Ce}5p_{1/2}$ lines in line with other work, although others have put it in between $\text{Ce}5p_{3/2}$ and $\text{Ce}5p_{1/2}$ energy position, based on relativistic computation of CeO_8 and $\text{Ce}_{63}\text{O}_{216}$ clusters³⁵. One of the motivations of the studies of O2s and Ce5p is charge transfer where these lines because of their quasi-degenerate energy positions are sensitive to the oxidation state of Ce cations. The spectra in Figure 4 are similar to those reported on a thin film of CeO_2 grown on Rh(111)³⁶ excited with photon energy equal to 125 eV (Ce4d-Ce4f resonance). The spectra are also similar to irradiated (with Xe ions) CeO_2 thin film and bulk³⁴. The authors pointed out the final state effect ($3d^94f^1\text{OVMO}^{-1}$ (outer valence molecular orbital, OVMO) and $3d^95p^5\text{np}^1$ (inner valence molecular orbital, INVO)). In another work³³, the authors indicated the Ce 5p atomic orbitals participate in the formation of both OVMO and IVMO where a large part of the latter is taken by the filled Ce $5p_{1/2}$, $5p_{3/2}$, and O 2s atomic shells.

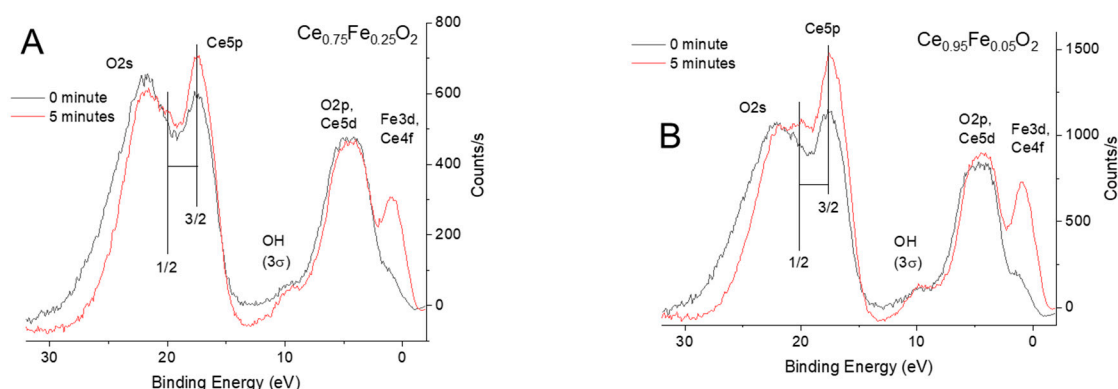


Figure 4. A. Normalized valence band-XPS and Ce5p, O2s and Ce5s of $\text{Ce}_{0.75}\text{Fe}_{0.25}\text{O}_2$ before (0 minute) and after 5 minutes Argon ions sputtering. B. Normalized valence band-XPS and Ce5p, O2s and Ce5s of $\text{Ce}_{0.95}\text{Fe}_{0.05}\text{O}_2$ before (0 minute) and after 5 minutes Argon ions sputtering. Note the change in intensity of the Ce5p when compared to the O2s.

The spectra of Figure 4 are fitted in SI Figure S2. Four peaks are considered (Ce5p_{3/2,1/2} and two for O2s). The two O2s peaks are for the two different (bulk and surface oxygen atoms) environments and are separated by about 2.5 eV (similar to the O1s signal). It is to be noted that similar attribution was given for the O2s of clean and glycine-dosed surfaces where the high binding O2s line is due to surface hydroxyls and carboxylates³⁷.

Figure 5 presents XPS Ce3d of Ce cations of the fresh and Ar ions reduced samples. The presence of both oxidation states of Ce cations is clear even in the freshly prepared oxides. However in this case Ce³⁺ cations concentration is small and most likely resides in deeper layers from the surface. In Figure 5 A and B) are shown the lines position and attribution (3d_{5/2}: u, u'' and u''' and 3d_{3/2}: v, v'' and v''' for Ce⁴⁺ cations and 3d_{5/2}: u_o, u' and 3d_{3/2}: v_o and v' for Ce³⁺ cations). Upon fitting for these peaks, information can be obtained. In Figure 5 and the inset table, a comparison between the fresh and the most reduced samples is made. The presence of Fe 5% resulted in a more pronounced Ce³⁺ concentration when compared to Fe 25%. This is in line with the valence band results presented in Figures 2 and 3. CeO₂ alone showed a very mild increase upon reduction; this is also in line with the virtually no change in the Ce5p/O2s lines in SI Figure 1. Ar ions sputtering relies on the momentum transfer of incoming ions (in this case 1 keV kinetic energy) that results in breaking the chemical bonds. As such there should be no difference between CeO₂ and Fe-substituted CeO₂ since the incoming ions have a much larger energy than the chemical bond, assuming complete energy transfer. However, this is a cascade reaction where the energy transfer occurs consecutively and therefore the last steps of an incoming ion (before it leaves the material or is implanted in it irreversibly) would be more efficient for weaker bonding. This is particularly important for polycrystalline nanoparticles where interparticle pore diffusion dominates.

Based on the Ce4f/O2p, Ce5p/O2s, and Ce3d (for Ce⁴⁺ and Ce³⁺) XPS signals, table 1 is constructed to provide an estimate of the reduction of Ce cations in this work.

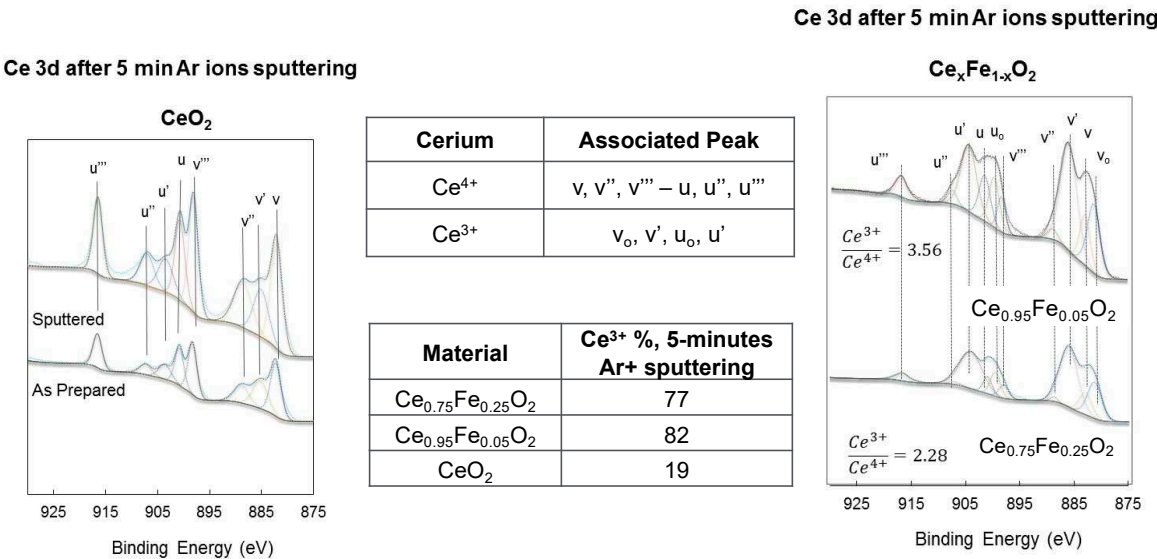


Figure 5. XPS Ce3d of as prepared CeO₂, Ce_{0.75}Fe_{0.25}O₂, and Ce_{0.95}Fe_{0.05}O₂ and after 5 minutes Ar ions sputtering. Also shown are the computed contribution of Ce³⁺ and Ce⁴⁺ cations.

Table 1. Extracted quantitative values from XPS Ce3d, Ce4f, Ce5p, Fe2p, and thermochemical water splitting to hydrogen over reduced oxides. The XPS data are those for reduced oxides upon 5 minutes of argon ions sputtering. The hydrogen production data are at 700°C under N₂ from prior hydrogen-reduced oxides at 700°C.

Oxide	Ce ³⁺ /Ce ⁴⁺ Ce3d	[Ce 4f + Fe 3d ^x]/O 2p	Fe ⁰ /Fe ³⁺ Fe2p	Ce 5p/O 2s	H ₂ production (mol/g)
CeO ₂	0.2	-	-	0	0.2 × 10 ⁻⁶
Ce _{0.75} Fe _{0.25} O ₂	2.3	0.3	0.5	1.6	7.4 × 10 ⁻⁶
Ce _{0.95} Fe _{0.05} O ₂	3.6	0.4	0.6	1.75	11.4 × 10 ⁻⁶

The XPS core levels of iron oxides are among the most studied oxides³⁸. There are three common oxidation states for the oxides, Fe³⁺ such as in Fe₂O₃, Fe²⁺ such as in FeO, and Fe₃O₄, in addition to metallic Fe. The spectra are complicated by the presence of satellites^{39,40,41}, iron hydroxide (FeOOH)^{42,43}, and many multiplets⁴⁴. The binding energy of XPS Fe2p is at about 707 eV for metallic iron, 710 eV for Fe²⁺, and 711 eV for Fe³⁺ cations. In the present study, a further complication arises from the presence of Ce Auger lines in the Fe2p region. Moreover, although a charge neutralization was used, the as-prepared oxide always had wider peaks when compared to that reduced upon ion sputtering. Therefore, peak areas are to be taken with an estimate of 20% errors and binding energies within 0.5 eV accuracy. Both oxides show very similar spectra and trends upon reduction. While as expected, the as-prepared oxides contained Fe³⁺ cations, they however contained Fe²⁺ and some metallic iron. Fe²⁺ might be formed upon the already reduced states during the preparation (Figure 6). The presence of metallic iron was not expected and is most likely due to interstitial atoms formed due to strong lattice distortion. The insets in both figures show the trend during the reduction. It was opted to subtract the Fe²⁺ and Fe⁰ contribution of the as-prepared oxides to see the trend. In both cases, the amount of Fe²⁺ increases, similar to a previous study⁴⁵, then decreases to zero indicating that within the reduction time studied all reducible Fe³⁺ cations were transformed to metallic Fe. In line with the valence band results, it appears that both Ce⁴⁺ and Fe³⁺ cations are more efficiently reduced when in small amounts (Fe_{0.05}) as seen in Figure 6 B, although the difference is not dramatic.

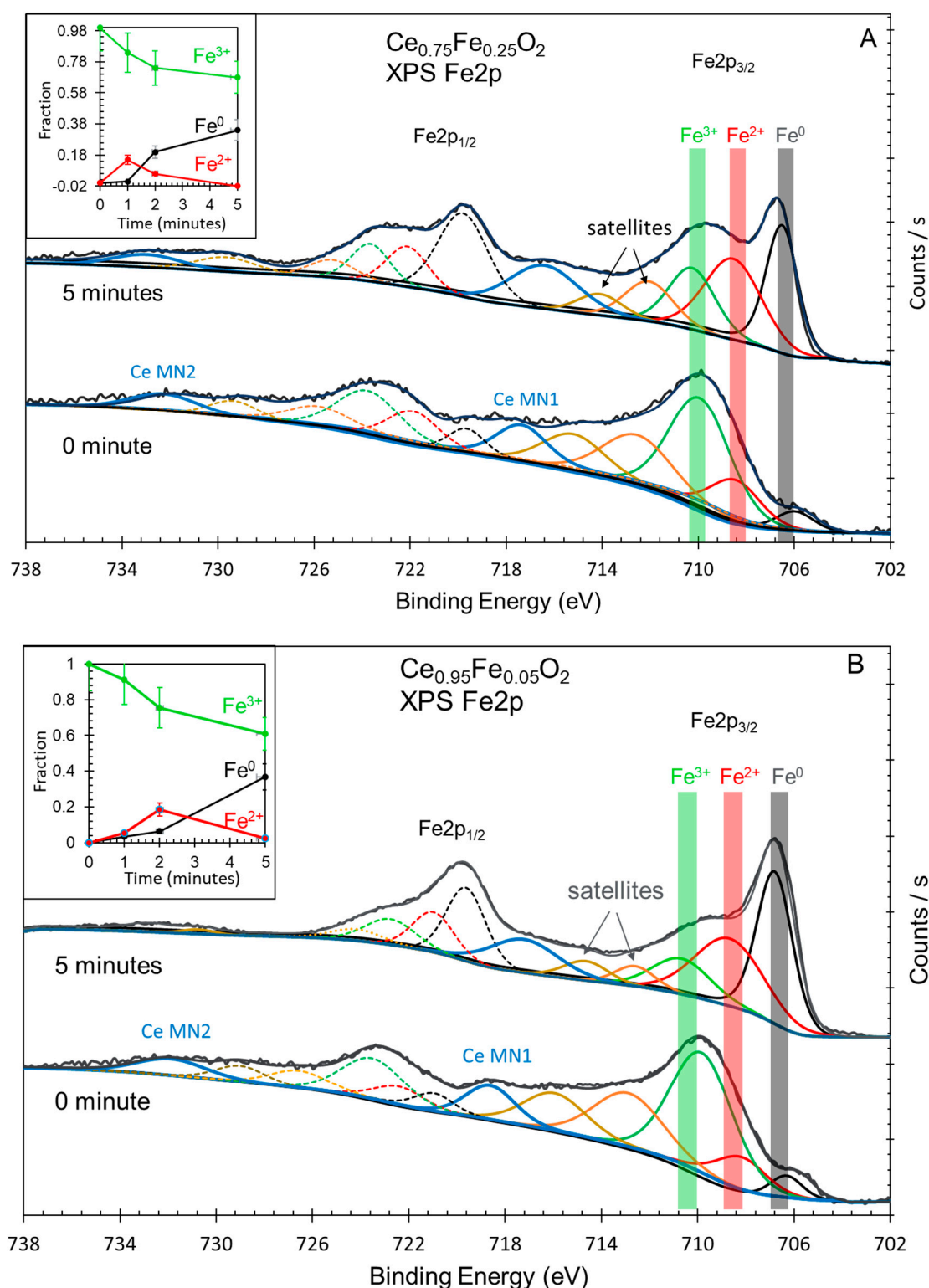


Figure 6. A. XPS Fe2p of as prepared $\text{Ce}_{0.75}\text{Fe}_{0.25}\text{O}_2$ and after 5-minute Ar ions sputtering. B. XPS Fe2p of as prepared $\text{Ce}_{0.95}\text{Fe}_{0.05}\text{O}_2$ and 5-minute Ar ions sputtering. Insets in A and B: quantitative analysis of XPS Fe2p of $\text{Ce}_{0.75}\text{Fe}_{0.25}\text{O}_2$ and $\text{Ce}_{0.95}\text{Fe}_{0.05}\text{O}_2$ before and after sputtering at the indicated time.

Figure 7 presents the hydrogen production of the three oxides from water at 700°C. The point in the figure is to relate the production to the observed reduced states of the oxides. Because as indicated the two mixed oxides are not segregated when heated to this temperature, the link to spectroscopic measurements would be relevant even though as such it is not practical (since the oxides were

previously reduced with molecular hydrogen). CeO_2 alone shows negligible activity while Fe-substituted cerium oxides are active (the production is given in Table 1). The activity of the $\text{Ce}_{0.95}\text{Fe}_{0.05}\text{O}_2$ is almost twice that of the $\text{Ce}_{0.75}\text{Fe}_{0.25}\text{O}_2$. This suggests that the activity is more linked to Ce^{3+} than to Fe^0 (based on XPS $\text{Ce}3d$, and XPS $\text{Ce}5p/\text{O}2s$). This is because the content of Fe^0 in both reduced oxides was similar (XPS $\text{Fe}2p$) while that of Ce^{3+} was higher for $\text{Ce}_{0.95}\text{Fe}_{0.05}\text{O}_2$ than for $\text{Ce}_{0.75}\text{Fe}_{0.25}\text{O}_2$.

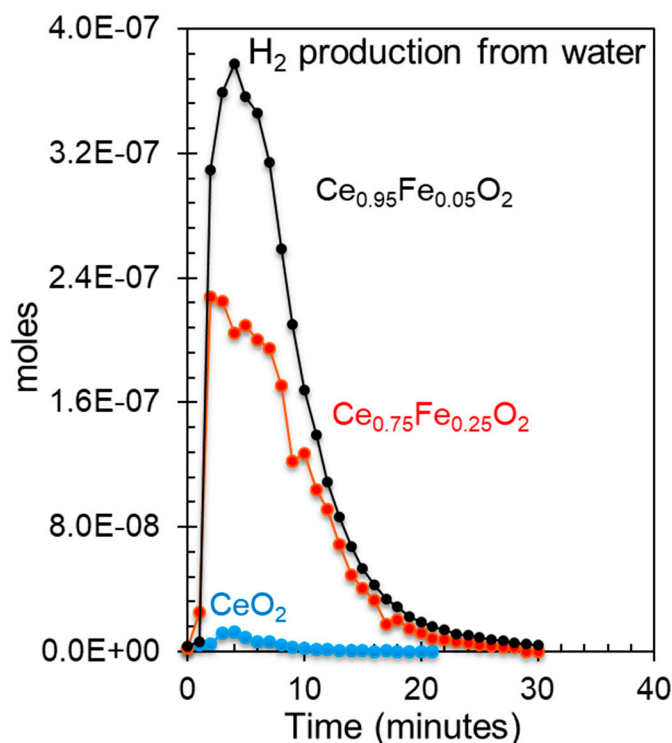


Figure 7. Hydrogen production from water over CeO_2 , $\text{Ce}_{0.75}\text{Fe}_{0.25}\text{O}_2$, and $\text{Ce}_{0.95}\text{Fe}_{0.05}\text{O}_2$ that were prior reduced with hydrogen at 700°C at one atmosphere.

4. Conclusions

In this work, the extent of reduction by Ar-ions sputtering of metal cations in CeO_2 , $\text{Ce}_{0.95}\text{Fe}_{0.05}\text{O}_2$, and $\text{Ce}_{0.75}\text{Fe}_{0.25}\text{O}_2$ is studied by core and valence level spectroscopy to link it to the increased reaction rates of the thermal water splitting when compared to CeO_2 alone. Ar ions sputtering resulted in an increase in the intensity of $\text{Ce}4f$ lines at about 1.5 eV below the Fermi level when compared to the $\text{O}2p$ lines. Moreover, the XPS $\text{Ce}5p/\text{O}2s$ ratio is found to be sensitive to the degree of reduction which is attributed to a higher charge transfer from the oxygen to Ce ions upon reduction. This increase is concomitant with the increase of the XPS $\text{Ce}3d$ of the fraction of Ce^{3+} . Both increases are found to be higher for reduced $\text{Ce}_{0.95}\text{Fe}_{0.05}\text{O}_2$ when compared to $\text{Ce}_{0.75}\text{Fe}_{0.25}\text{O}_2$. On the other hand, the XPS $\text{Fe}2p$ showed no preferential increase between the two mixed oxides. Because water splitting to molecular hydrogen was found to be higher on $\text{Ce}_{0.95}\text{Fe}_{0.05}\text{O}_2$ than on $\text{Ce}_{0.75}\text{Fe}_{0.25}\text{O}_2$, it is postulated that the active sites for the reaction are those of Ce^{3+} cations and not metallic Fe.

Supplementary Materials: The following supporting information can be downloaded at the website of this paper posted on Preprints.org.

Acknowledgments: The author thanks Mr. Yahya Al-Salik (SABIC, STC-KAUST) for preparing the mixed oxides and for his technical help throughout the study and Dr. Toseef Ahmed (SABIC, STC-Riyadh) for the XPS data acquisition.

References

1. Trovarelli, A. Catalytic Properties of Ceria and CeO₂-Containing Materials. *Catalysis Reviews Science and Engineering* **1996**, *38*, 439-520.
2. Yang, C.; Lu, Y.; Zhang, L.; Kong, Z.; Yang, T.; Tao, L.; Zou, Y.; Wang, S. Defect Engineering on CeO₂-Based Catalysts for Heterogeneous Catalytic Applications, *Small Struct.* **2021**, *2*, 2100058 (1-25).
3. Torrente-Murciano, L.; Garcia-Garcia, R. R. Effect of nanostructured support on the WGS activity of Pt/CeO₂ catalysts., *Catalysis Communications*, **2015**, *71*, 1-6.
4. Idriss, H. Oxygen vacancies role in thermally driven and photon driven catalytic reactions. *Chem. Catalysis* **2022**, *2*, 1549-1560.
5. Onigbajumo, A.; Swarnkar, P.; Will, G.; Sundararajan, T.; Taghipour, A.; Couperthwaite, S.; Steinberg, T.; Rainey, T. Techno-economic evaluation of solar-driven ceria thermochemical water-splitting for hydrogen production in a fluidized bed reactor. *Journal of Cleaner Production*, **2022**, *371*, 133303.
6. Chueh, W. C.; Falter, C.; Abbott, M.; Scipio, D.; Furler, Haile, S. M.; Steinfeld, A. High-flux solar-driven thermochemical dissociation of CO₂ and H₂O using nonstoichiometric ceria. *Science*, **2010**, *330*, 797-801.
7. Alifanti, M.; Baps, B.; Blangenois, N.; Naud, J.; Grange, P.; Delmon, B. Characterization of CeO₂-ZrO₂ Mixed Oxides. Comparison of the Citrate and Sol-Gel Preparation Methods. *Chem. Mater.* **2003**, *15*, 395-403.
8. Andersson, D.A.; Simak, S. I.; Skorodumova, N. V.; Abrikosov, I.A., Johansson, B. Redox properties of CeO₂-MO₂ (M = Ti, Zr, Hf, or Th) solid solutions from first principles calculations. *Appl Phys Lett.* **2007**, *90*, 031909.
9. Diagne, C.; Idriss, H.; Kiennemann, A. Hydrogen Production by Ethanol Reforming over Rh/CeO₂-ZrO₂ Catalysts., *Catal. Commun.* **2002**, *3*, 565-571.
10. Grau-Crespo, R.; de Leeuw, N. H.; Hamad, S.; Waghmare, U. V. Phase separation and surface segregation in ceria-zirconia solid solutions. *Proc. R. Soc. A* **2011**, *467*, 1925-1938.
11. Hanken, B. E.; Stanek, C.R.; Grønbech-Jensen, N.; Asta, M. Computational study of the energetics of charge and cation mixing in U_{1-x}Ce_xO₂. *Phys. Rev. B* **2011**, *84*, 085131.
12. Scaranto, G.; Idriss, H. The Effect of Uranium Cations on the Redox Properties of CeO₂ Within the Context of Hydrogen Production from Water. *Top. Catal.* **2015**, *58*, 143-148.
13. Al-Shankiti, I.; Al-Otaibi, F.; Al-Salik, Y.; Idriss, H. Solar thermal hydrogen production from water over modified CeO₂ materials. *Top. Catal.* **2013**, *56*, 1129-1138.
14. Prieur, D.; Vigier, J.-F.; Popa, K.; Walter, O.; Dieste, O.; Varga, Z.; Beck, A.; Vitova, T.; Scheinost, A.; Martin, P. Charge distribution in U_{1-x}Ce_xO_{2+y} nanoparticles. *Inorganic Chemistry* **2021**, *60*, 14550-14556.
15. Gupta, A.; Waghmare, U. V.; Hegde, M. S. Correlation of Oxygen Storage Capacity and Structural Distortion in Transition-Metal-, Noble-Metal-, and Rare-Earth-Ion-Substituted CeO₂ from First Principles Calculation. *Chem. Mater.* **2010**, *22*, 5184-5198.
16. Gupta, A.; Kumar, A.; Waghmare, U. V.; Hegde, M. S. Origin of activation of Lattice Oxygen and Synergistic Interaction in Bimetal-Ionic Ce_{0.89}Fe_{0.1}Pd_{0.01}O_{2-δ} Catalyst. *Chem. Mater.* **2009**, *21*, 4880-4891.
17. Al-Taweel, S.; Nadeem, M. A.; Idriss, H. A study of Ce_xFe_{1-x}O₂ as a reducible oxide for the thermal hydrogen production from water. *Energy Technology*, **2022**, 2100491 (1-9).
18. Cheng, L.; Yue, X.; Fan, J.; Xiang, Q. Site-Specific Electron-Driving Observations of CO₂-to-CH₄ Photoreduction on Co-Doped CeO₂/Crystalline Carbon Nitride S-Scheme Heterojunctions. *Adv. Mater.* **2022**, *34*, 2200929 (1-11).
19. Zhao, S.; Kang, D.; Liu, Y.; Wen, Y.; Xie, X.; Yi, H.; Tang, X. Spontaneous Formation of Asymmetric Oxygen Vacancies in Transition-Metal-Doped CeO₂ Nanorods with Improved Activity for Carbonyl Sulfide Hydrolysis. *ACS Catal.* **2020**, *10*, 11739-11750.
20. He, W.; Ran, J.; Yang, G.; He, Z.; Huang, X.; Crittenden, J. Promoting effect of Co-doped CeO₂ nanorods activity and SO₂ resistance for Hg⁰ removal. *Fuel* **2022**, *317*, 123320 (1-9).
21. Ahn, K.; Yoo, D. S.; Prasad, D. H.; Lee, H.-W.; Chung, Y.-C.; Lee, J.-H. Role of Multivalent Pr in the Formation and Migration of Oxygen Vacancy in Pr-Doped Ceria: Experimental and First-Principles Investigations. *Chem. Mater.* **2012**, *24*, 4261-4267.
22. Zhang, M.; Jiang, D.; Jiang, H. Enhanced oxygen storage capacity of Ce_{0.88}Mn_{0.12}O_y compared to CeO₂: An experimental and theoretical investigation. *Materials Research Bulletin* **2012**, *47*, 4006-4012.
23. Krcha, M. D.; Janik, M. J. Examination of Oxygen Vacancy Formation in Mn-Doped CeO₂ (111) Using DFT+U and the Hybrid Functional HSE06., *Langmuir* **2013**, *29*, 10120-10131.

24. Righi, G.; Benedetti, S.; Rita Magri, R. Investigation of the structural and electronic differences between silver and copper doped ceria using the density functional theory. *J. Phys.: Condens. Matter* **2022**, *34*, 204010 (10pp).
25. Nolan, M. Enhanced oxygen vacancy formation in ceria (111) and (110) surfaces doped with divalent cations. *J. Mater. Chem.* **2011**, *21*, 9160-9168.
26. Wang, X.; Shen, M.; Wang, J.; Fabris, S. Enhanced Oxygen Buffering by Substitutional and Interstitial Ni Point Defects in Ceria: A First-Principles DFT+U Study. *J. Phys. Chem. C* **2010**, *114*, 10221–10228.
27. Grieshammer, S.; Grope, B. O. H.; Koettgen, J.; Martin, M. A combined DFT + U and Monte Carlo study on rare earth doped ceria. *Phys. Chem. Chem. Phys.* **2014**, *16*, 9974–9986.
28. Wang, H.; Qu, Z.; Xie, H.; Maeda, N.; Miao, L.; Wang, Z. Insight into the mesoporous $\text{Fe}_x\text{Ce}_{1-x}\text{O}_{2-x}$ catalysts for selective catalytic reduction of NO with NH_3 : Regulable structure and activity. *Journal of Catalysis* **2016**, *338*, 56–67.
29. Liu, X.-S.; Wang, X.-D.; Yao, M.; Cui, W.; Yan, H. Effects of Fe doping on oxygen vacancy formation and CO adsorption and oxidation at the ceria(111) surface. *Catalysis Communications* **2015**, *63*, 35–40.
30. Lykaki, M.; Stefa, S.; Carabineiro, S. A. C.; Pandis, P. K.; Stathopoulos, V. N.; Konsolakis, M. Facet-Dependent Reactivity of $\text{Fe}_2\text{O}_3/\text{CeO}_2$ Nanocomposites: Effect of Ceria Morphology on CO Oxidation. *Catalysts* **2019**, *9*, 371 (1-21).
31. Kaneko, H.; Miura, T.; Ishihara, H.; Taku, S.; Yokoyama, T.; Nakajima, H.; Tamaura, Y. Reactive ceramics of $\text{CeO}_{2-x}\text{MO}_x$ (M=Mn, Fe, Ni, Cu) for H_2 generation by two-step water splitting using concentrated solar thermal energy. *Energy* **2007**, *32*, 656–663.
32. Liang, C.; Ma, Z.; Lin, H.; Ding, L.; Qiu, J.; Frandsen, W.; Su, D. Template preparation of nanoscale $\text{Ce}_x\text{Fe}_{1-x}\text{O}_2$ solid solutions and their catalytic properties for ethanol steam reforming. *J. Mater. Chem.* **2009**, *19*, 1417–1424.
33. Metal Oxide Nanostructures Chemistry: Synthesis from Aqueous Solutions. Second Edition. Jean-Pierre Jolivet, Oxford University Press (2015) Editions EDP Sciences. Chapter 5, Surface Chemistry and Physicochemistry of Oxides, 181-226. DOI:10.1093/oso/9780190928117.003.0005
34. Maslakov, K. I.; Teterin, Y. A.; Popel, A. J.; Teterin, A. Y.; Ivanov, K. E.; Kalmykov, S. N.; Petrov, V. G.; Petrov, P. K.; Farnan, I. XPS study of ion irradiated and unirradiated CeO_2 bulk and thin film Samples. *Applied Surface Science* **2018**, *448*, 154–162
35. Maslakov, K. I.; Teterin, Y. A.; Ryzhkov, M. V.; Ivanov, K. E.; Popel, A. J.; Teterin, A. Y.; Kalmykov, S. N.; Petrov, V. G.; Petrov, P. K.; Farnan, I. The electronic structure and the nature of the chemical bond in CeO_2 . *Phys. Chem. Chem. Phys.* **2018**, *20*, 16167-16175.
36. Eck, S.; Castellarin-Cudia, C.; Surnev, S.; Ramsey, M. G.; Netzer, F. P. Growth and thermal properties of ultrathin cerium oxide layers on Rh(111). *Surface Science* **2002**, *520*, 173–185
37. Soria, E.; Román, E.; Williams, E. M.; de Segovia, J. L. Observations with synchrotron radiation (20–120 eV) of the $\text{TiO}_2(110)$ –glycine interface. *Surface Science* **1999**, *433–435*, 543–548.
38. Parkinson, G. S. Iron oxide surfaces. *Surface Science Reports* **2016**, *71*, 272–365
39. Mansour, A. N.; Brizzolara, R. A. Characterization of the Surface of FeO Powder by XPS. *Surf. Sci. Spectra* **1996**, *4*, 345–350.
40. Preisinger, M.; Krispin, M.; Rudolf, T.; Horn, S.; Strongin, D. R. Electronic structure of nanoscale iron oxide particles measured by scanning tunneling and photoelectron spectroscopies. *Phys. Rev. B* **2005**, *71*, 165409, 1-6.
41. Radu, T.; Iacovita, C.; Benea, D.; Turcu, R. X-Ray Photoelectron Spectroscopic Characterization of Iron Oxide Nanoparticles. *Applied Surface Science* **2017**, *405*, 337–343.
42. Grosvenor, A. P.; Kobe, B. A.; McIntyre, N. S. Studies of the oxidation of iron by water vapour using X-ray photoelectron spectroscopy and QUASES. *Surface Science* **2004**, *572*, 217–227.
43. Temesghen, W.; Sherwood, P. M. A. Analytical utility of valence band X-ray photoelectron spectroscopy of iron and its oxides, with spectral interpretation by cluster and band structure calculations. *Anal Bioanal Chem* **2002**, *373*, 601–608.

44. Bagus, P. S.; Nelin, C. J.; Brundle, C. R.; Vincent Crist, C. B.; Lahiri, N.; Rosso, K. M. Combined multiplet theory and experiment for the Fe 2p and 3p XPS of FeO and Fe₂O₃. *J. Chem. Phys.* **2021** 154, 094709.
45. Fondell, M.; Gorgoi, M.; Boman, M.; Lindblad, A. Surface modification of iron oxides by ion bombardment – Comparing depth profiling by HAXPES and Ar ion sputtering. *Journal of Electron Spectroscopy and Related Phenomena* **2018**, 224, 23–26.

Disclaimer/Publisher's Note: The statements, opinions and data contained in all publications are solely those of the individual author(s) and contributor(s) and not of MDPI and/or the editor(s). MDPI and/or the editor(s) disclaim responsibility for any injury to people or property resulting from any ideas, methods, instructions or products referred to in the content.